

Innate and adaptive lymphocytes sequentially shape the gut microbiota and lipid metabolism

Kairui Mao¹, Antonio P. Baptista¹, Samira Tamoutounour², Lenan Zhuang³, Nicolas Bouladoux², Andrew J. Martins⁴, Yuefeng Huang⁵, Michael Y. Gerner⁶, Yasmine Belkaid² & Ronald N. Germain¹

The mammalian gut is colonized by numerous microorganisms collectively termed the microbiota, which have a mutually beneficial relationship with their host^{1–3}. Normally, the gut microbiota matures during ontogeny to a state of balanced commensalism marked by the absence of adverse inflammation^{4,5}. Subsets of innate lymphoid cells (ILCs) and conventional T cells are considered to have redundant functions in containment and clearance of microbial pathogens^{6,7}, but how these two major lymphoid-cell populations each contribute to shaping the mature commensal microbiome and help to maintain tissue homeostasis has not been determined. Here we identify, using advanced multiplex quantitative imaging methods, an extensive and persistent phosphorylated-STAT3 signature in group 3 ILCs and intestinal epithelial cells that is induced by interleukin (IL)-23 and IL-22 in mice that lack CD4⁺ T cells. By contrast, in immune-competent mice, phosphorylated-STAT3 activation is induced only transiently by microbial colonization at weaning. This early signature is extinguished as CD4⁺ T cell immunity develops in response to the expanding commensal burden. Physiologically, the persistent IL-22 production from group 3 ILCs that occurs in the absence of adaptive CD4⁺ T-cell activity results in impaired host lipid metabolism by decreasing lipid transporter expression in the small bowel. These findings provide new insights into how innate and adaptive lymphocytes operate sequentially and in distinct ways during normal development to establish steady-state commensalism and tissue metabolic homeostasis.

To study the state and activity of innate and adaptive immune cells *in situ* in the context of the microbiota, we used quantitative multiplex immunohistochemistry (histo-cytometry)^{8–10}. Staining for both cell phenotype and molecules that indicate active cytokine signalling enabled us to simultaneously examine the cell distribution, cytokine production and topography of cytokine responses in a complex tissue. Because many relevant cytokines induce phosphorylation of STAT3¹¹, we focused on the presence and distribution of phosphorylated STAT3 (pSTAT3) in the distal small intestine of animals with an intact (wild type) or adaptive-lymphocyte-deficient (*Rag1*^{-/-}) immune system under specific pathogen-free conditions. Using this approach, we observed substantial pSTAT3 in both CD3⁻ROR γ t⁺-group 3 innate lymphoid cells (ILC3s) and nearly all EpCAM⁺ intestinal epithelial cells (IECs) in the distal small intestine of *Rag1*^{-/-} but not wild-type mice (Fig. 1a). ROR γ t⁺ ILC3s occur as a number of subpopulations with different locations in the gut: CCR6⁺ lymphoid-tissue inducer-like ILC3s reside mainly in cryptopatches and isolated lymphoid follicles, while NKp46⁺ ILC3s and NKp46⁻ ILC3s are mostly located in the lamina propria¹². ILC3s in both locations were equally activated in *Rag1*^{-/-} mice (Fig. 1a, b and Extended Data Fig. 1). Because the small intestine is colonized with commensal microbiota, we examined

whether these microorganisms had a role in the pSTAT3 signature by treating specific pathogen-free *Rag1*^{-/-} mice with broad-spectrum antibiotics or using germ-free *Rag1*^{-/-} mice. All pSTAT3 signals in ILC3s and IECs were eliminated in these mice (Fig. 1c, d). Segmented filamentous bacteria (SFB) attach directly to IECs in the distal small intestine and contribute to T_H17 cell differentiation and ILC3 activation *in vivo*^{13,14}. We therefore mono-colonized germ-free *Rag1*^{-/-} mice with SFB, which resulted in robust STAT3 activation in ILC3s and IECs (Fig. 1c, d). We conclude that STAT3 phosphorylation in ILC3s and IECs arises from signalling induced by microbiota, and that defined microbes such as SFB have a major role in this signalling in *Rag1*^{-/-} mice.

IL-23 and IL-22 are functionally linked cytokines with the potential to induce pSTAT3 in ILC3s and IECs, respectively^{15,16}. We therefore examined pSTAT3 in *Rag1*^{-/-} mice that were also deficient in *Il23a* (which codes for the IL-23p19 subunit) or *Il22*. In the absence of IL-23, pSTAT3 was no longer detected in ILC3s or IECs. By contrast, *Il22*^{-/-}*Rag1*^{-/-} mice had a similar proportion of pSTAT3⁺ ILC3s as *Rag1*^{-/-} mice, but lacked pSTAT3⁺ IECs. The pSTAT3 signature in ILC3s and IECs was independent of IL-6 (Extended Data Fig. 2a, b). These data reveal that pSTAT3 generation in ILC3s depends on IL-23 but not on IL-6 or IL-22, whereas pSTAT3 in IECs depends on both IL-23 and IL-22. Because ILC3s and not IECs express the IL-23 receptor, it seemed likely that STAT3 activation in ILC3s and IECs were sequential events downstream of IL-23 and IL-22, respectively. To test this hypothesis, we examined *Rorc*(γ t)^{GFP/GFP}*Rag1*^{-/-} mice, which specifically lack ILC3s. The absence of pSTAT3 in IECs of these mice suggests that ILC3s are critical for STAT3 activation in epithelial cells in the small intestine of *Rag1*^{-/-} mice (Extended Data Fig. 2c). Examination of *Rag1*^{-/-} mice expressing an *Il22*-tdTomato reporter showed that pSTAT3⁺ ILC3s produced IL-22 (Extended Data Fig. 2d). To investigate the source of IL-23, we isolated different myeloid-cell populations from the small intestine of wild-type and *Rag1*^{-/-} mice¹⁷ (Extended Data Fig. 3a). CD11b⁺ conventional dendritic cells, as well as CCR2⁺ monocytes and monocyte-derived dendritic cells, can all express *Il23a*, but CCR2⁺ cells from *Rag1*^{-/-} mice had higher *Il23a* expression than those from wild-type mice, whereas there was no significant difference in *Il23a* expression in the CD11b⁺ populations (Extended Data Fig. 3b). To determine whether IL-23 production from CCR2⁺ myeloid cells was responsible for the pSTAT3 signature in *Rag1*^{-/-} mice, we depleted these cells by injecting these mice with a CCR2 antibody. After two weeks, there were no pSTAT3⁺ ILC3s or IECs in antibody-treated *Rag1*^{-/-} mice (Extended Data Fig. 3c), which indicates that IL-23 production in CCR2⁺ cells is critical for STAT3 activation in the small intestine of *Rag1*^{-/-} mice. Similar results were obtained using a more broadly depleting antibody against GR1 (Extended Data Fig. 3c).

¹Lymphocyte Biology Section, Laboratory of Systems Biology, National Institute of Allergy and Infectious Disease, National Institutes of Health, Bethesda, Maryland 20892, USA. ²Mucosal Immunology Section, Laboratory of Parasitic Diseases, National Institute of Allergy and Infectious Diseases, National Institutes of Health, Bethesda, Maryland 20892, USA. ³Laboratory of Endocrinology and Receptor Biology, National Institute of Diabetes and Digestive and Kidney Diseases, National Institutes of Health, Bethesda, Maryland 20892, USA. ⁴Systems Genomics and Bioinformatics Unit, Laboratory of Systems Biology, National Institute of Allergy and Infectious Disease, National Institutes of Health, Bethesda, Maryland 20892, USA. ⁵Laboratory of Immunology, National Institute of Allergy and Infectious Diseases, National Institutes of Health, Bethesda, Maryland 20892, USA. ⁶Department of Immunology, University of Washington School of Medicine, Seattle, Washington 98109, USA.

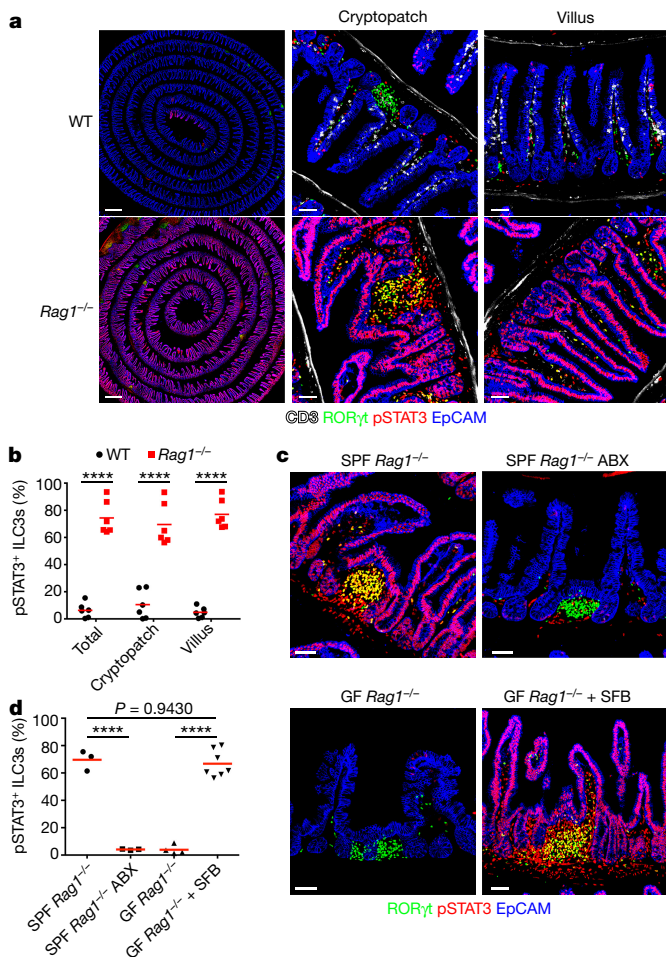


Figure 1 | pSTAT3⁺ ILC3s and IECs induced by microbiota in small intestine of *Rag1*^{-/-} mice. **a–d**, Immunofluorescence staining of ileum (**a**, **c**) and quantification of pSTAT3⁺ ILC3s (**b**, **d**) from wild-type (WT) or *Rag1*^{-/-} mice ($n = 6$; **a**, **b**), and from specific pathogen-free (SPF) *Rag1*^{-/-} mice with or without antibiotics treatment ($n = 3$), germ-free *Rag1*^{-/-} mice ($n = 4$) and germ-free *Rag1*^{-/-} mice mono-colonized with SFB ($n = 7$; **c**, **d**). ABX, antibiotics; GF, germ-free. Results are representative of two (**c**, **d**) or three (**a**, **b**) independent experiments. Bars indicate mean; **** $P < 0.0001$, otherwise exact P values are shown; two-tailed Student's t -test (**b**) or one-way ANOVA (**d**). Scale bars, 50 μm (except **a**, left, 500 μm).

Together, IL-23 and IL-22 constitute a circuit that involves ILC3s and produces strong signalling in IECs in animals that lack an adaptive immune system. Though such a circuit was previously reported upon pathogen infection of *Rag1*-deficient mice¹⁵, these new findings show that ILC3s and IECs are robustly and persistently activated by the commensal microbiota in the absence of adaptive immunity.

Responses to microbes typically involve sequential activity of the innate and then adaptive immune systems. However, whether ILC responses that are thought to qualitatively parallel those of CD4⁺ T cells with which they share master transcription factor expression (for example, ROR γ t expression) operate sequentially or in parallel is unknown. The difference in IL-22-dependent IEC signalling between wild-type and *Rag1*^{-/-} adult mice suggested that in wild-type mice, innate cells might be activated by the microbiota before an effective adaptive immune response develops. To explore this possibility, we examined ileal pSTAT3 in wild-type and *Rag1*^{-/-} progeny of SFB⁺ mothers. In neonatal mice, which have a less diverse microbiota and limited SFB colonization¹⁸, neither wild-type nor *Rag1*^{-/-} mice had pSTAT3⁺ ILC3s or IECs. However, shortly after weaning, when bacterial colonization and expansion of the SFB population occurs, there was substantial activation of ILC3s and STAT3 signalling in

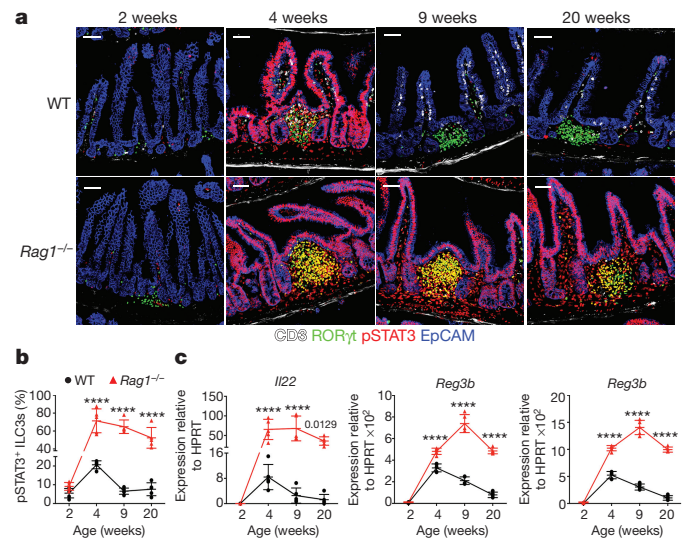


Figure 2 | Transient activation of ILC3s and IECs shortly after weaning in wild-type mice. **a**, Immunofluorescence staining of ileum from wild-type and *Rag1*^{-/-} mice at the indicated ages ($n = 5$). **b**, Quantification of pSTAT3⁺ ILC3s in **a**. **c**, Expression of the indicated genes in the ileum from mice as in **a** ($n = 5$). Results are representative of two independent experiments. Mean \pm s.d.; **** $P < 0.0001$, otherwise exact P values are shown; two-way ANOVA. Scale bars, 50 μm .

IECs in wild-type mice, although this was less robust than in *Rag1*^{-/-} mice (Fig. 2a, b). As the adaptive immune system of wild-type mice matured, ILC3s were no longer activated, whereas the activation persisted at high levels in ILC3s in *Rag1*^{-/-} mice (Fig. 2a, b). Expression of *Il22* and host-defence genes correlated precisely with ILC3 activation (Fig. 2c). These data indicate that during ontogeny, innate lymphoid cells operate before the adaptive system has fully developed^{19,20}. The emerging adaptive response then largely silences the ILC response and establishes a homeostatic state of non-inflammatory commensalism. Notably, the absence of the pSTAT3 signature in IECs from adult wild-type mice indicates that the effector mechanisms of the adaptive immune response to commensals is mechanistically distinct from that of ILC3s and that the existing paradigm that equates the effector functions of ILCs with subsets of CD4⁺-effector-T cells is not universally applicable^{21,22}.

To study the potentially distinct effects of innate and adaptive lymphocytes on the microbiota, we measured the abundance of different bacterial species in the small intestines of co-housed wild-type, *Rag1*^{-/-} and *Il23a*^{-/-} *Rag1*^{-/-} mice. In the absence of adaptive immunity, most bacteria, including SFB, were increased in *Rag1*^{-/-} mice. However, in the absence of STAT3 activation, SFB abundance was further increased in *Il23a*^{-/-} *Rag1*^{-/-} mice (Extended Data Fig. 4a). Although both innate and adaptive lymphocytes control the quantity of SFB, scanning electron microscopy revealed that SFB have markedly different morphology depending on whether adaptive lymphocytes are present. In the ileum of *Rag1*^{-/-} mice, activated ILC3s prevented development of SFB into long filamentous forms, and the adaptive lymphocytes limited the number of SFB that attached to epithelial cells (Extended Data Fig. 4b, c). These findings show that innate and adaptive lymphocytes adopt different strategies to regulate the commensal state, with the activity of adaptive lymphocytes dominating over that of innate lymphoid cells under these conditions.

We next investigated which host adaptive immune cells prevent ILC3 activation and epithelial-cell signalling. First, we compared the distribution of pSTAT3 in the ileum of wild-type, *Rag1*^{-/-}, *Tcra*^{-/-} (T cell-deficient) and *Ighm*^{-/-} (B cell-deficient) mice. Neither T cell nor B cell-deficient mice had pSTAT3⁺ ILC3s or IECs (Extended Data Fig. 5a, b). As the pSTAT3 signature in *Rag1*^{-/-} mice depended

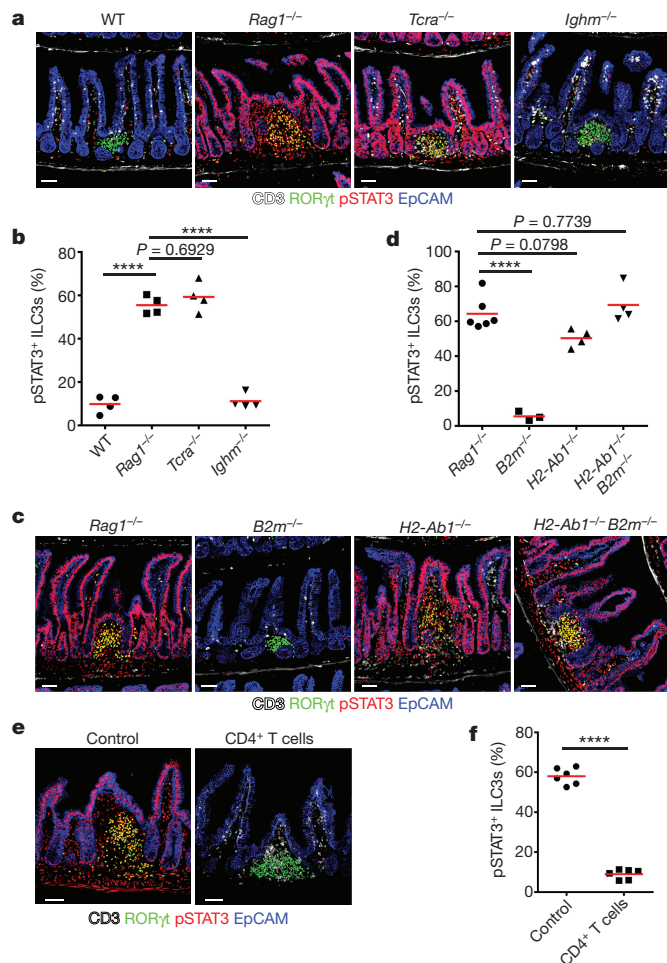


Figure 3 | Role of CD4⁺ T cells in controlling ILC3 and IEC activation. Immunofluorescence staining of ileum (a, c and e) and quantification of pSTAT3⁺ ILC3s (b, d and f) from co-housed wild-type, *Rag1*^{-/-}, *Tcrα*^{-/-} and *Ighm*^{-/-} mice (*n* = 4; a, b); co-housed *Rag1*^{-/-} (*n* = 6), *B2m*^{-/-} (*n* = 3), *H2-Ab1*^{-/-} (*n* = 4) and *H2-Ab1*^{-/-}*B2m*^{-/-} (*n* = 4) mice (c, d); and *Rag1*^{-/-} mice (*n* = 6) or *Rag1*^{-/-} mice with adoptive transfer of CD4⁺ T cells (*n* = 6; e, f). Results are representative of two independent experiments. Bars indicate mean; *****P* < 0.0001, otherwise exact *P* values are shown; one-way ANOVA (b, d) or two-tailed Student's *t*-test (f). Scale bars, 50 μm.

on specific bacteria such as SFB (Fig. 1c), we co-housed wild-type, *Rag1*^{-/-}, *Tcrα*^{-/-} and *Ighm*^{-/-} mice for 4–6 weeks and examined STAT3 phosphorylation in these animals. After co-housing, ILC3s and IECs from *Tcrα*^{-/-} mice but not *Ighm*^{-/-} mice showed strong STAT3 phosphorylation (Fig. 3a, b), consistent with a change in the abundance of SFB in the co-housed *Tcrα*^{-/-} mice (Extended Data Fig. 5c). These data show that αβ-T cells are critical for preventing ILC3 activation and IEC signalling induced by SFB. As the presence of SFB was critical for the pSTAT3 signature, all the mice used in the following experiments were co-housed with *Rag1*^{-/-} mice unless otherwise noted.

To identify whether CD4⁺ helper or CD8⁺ cytotoxic cells were responsible for inhibiting ILC3 activation, we examined STAT3 activation in MHCII-deficient (*H2-Ab1*^{-/-}), MHCI-deficient (*B2m*^{-/-}) and MHCI and MHCII-double-deficient (*H2-Ab1*^{-/-}*B2m*^{-/-}) mice, which specifically lack CD4⁺ T cells, CD8⁺ T cells or both, respectively. After co-housing with *Rag1*^{-/-} mice, both *H2-Ab1*^{-/-} and *H2-Ab1*^{-/-}*B2m*^{-/-} mice had pSTAT3⁺ ILC3s and IECs, whereas the equivalent cells in *B2m*^{-/-} mice were pSTAT3⁻ (Fig. 3c, d). To investigate whether CD4⁺ T cells were sufficient to suppress ILC3 activation, we adoptively transferred total CD4⁺ T cells into *Rag1*^{-/-} mice and

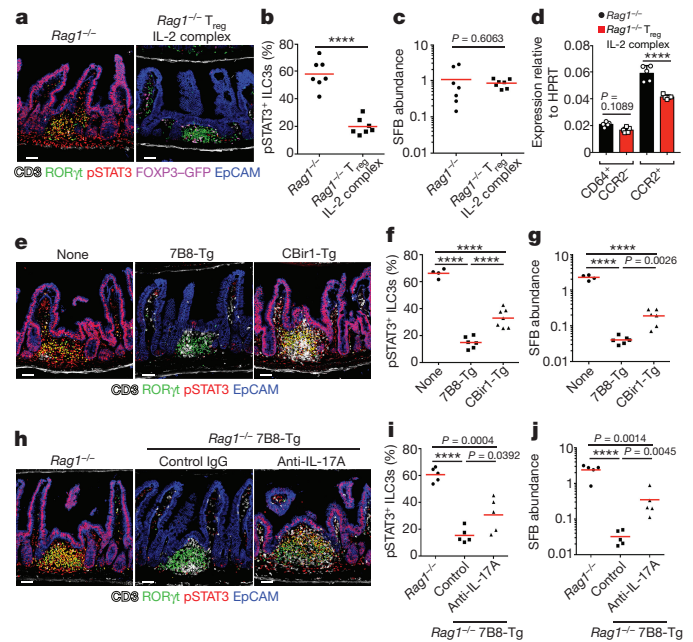


Figure 4 | Suppression of ILC3 activation by T_{reg} and T_H17 cells. a–c, Immunofluorescence staining of ileum (a) and quantification of pSTAT3⁺ ILC3s (b) and SFB (c) from the small intestine of *Rag1*^{-/-} mice (*n* = 7) or *Rag1*^{-/-} mice with adoptive transfer of CD4⁺ FOXP3–GFP⁺ T_{reg} cells treated with IL-2–IL-2-antibody complexes (*n* = 7). d, Expression of *Il23p19* in CD64⁺ CCR2⁻ macrophages (*n* = 5) and CCR2⁺ myeloid cells (*n* = 5) from small intestine of mice as in a. e–j, Immunofluorescence staining of ileum (e, h) and quantification of pSTAT3⁺ ILC3s (f, i) and SFB (g, j) in distal small intestine of *Rag1*^{-/-} mice (*n* = 4) and *Rag1*^{-/-} mice with adoptive transfer of 7B8–Tg T cells (*n* = 6) or CBir1–Tg T cells (*n* = 7) (e–g), and *Rag1*^{-/-} mice (*n* = 5) and *Rag1*^{-/-} mice with adoptive transfer of 7B8–Tg T cells treated with anti-IL-17A antibody (two independent experiments, *n* = 5) or control antibody (two independent experiments, *n* = 5) (h–j). Results are representative of two independent experiments. Bars show mean (b, c, f, g, i and j) or mean ± s.d. (d). *****P* < 0.0001, otherwise exact *P* values are shown; two-tailed Student's *t*-test (b–d) or one-way ANOVA (f, g, i and j). Scale bars, 50 μm.

found that they prevented STAT3 phosphorylation in ILC3s and IECs (Fig. 3e, f). Reduction of ILC3 activity by CD4⁺ T cells has been reported previously²³, but the mechanism was not addressed. FOXP3⁺ T_{reg} and T_H17 cells are the most abundant subsets of CD4⁺ T cells in the intestinal lamina propria²⁴. To examine the possible role of T_{reg} cells, we isolated these cells from *Foxp3*^{GFP} mice and transferred them into *Rag1*^{-/-} mice along with IL-2–IL-2-antibody complexes to maintain their number and function^{10,25}. Six to eight weeks after transfer, SFB abundance in the small intestine of these mice had not changed, but pSTAT3 in ILC3s and IECs was diminished (Fig. 4a–c). This effect was concordant with reduced *Il23a* expression in CCR2⁺ myeloid-cell populations (Fig. 4d). SFB preferentially induces antigen-specific effector CD4⁺ T_H17 cells^{19,20}. To examine the role of T_H17 cells in controlling ILC3 activation, we took advantage of SFB-specific T cell receptor transgenic mice (7B8–Tg). Adoptive transfer of naive 7B8–Tg CD4⁺ T cells into *Rag1*^{-/-} recipients markedly decreased SFB abundance in the small intestine, limiting ILC3 activation. By comparison, CBir1–Tg CD4⁺ T cells, which recognize commensal-derived flagellin, had only a modest effect on the abundance of SFB and ILC3 activation (Fig. 4e–g). Treatment with IL-17A-neutralizing antibodies partially reversed the effect of 7B8–Tg cells on ILC3 activation and SFB reduction; the incomplete nature of this effect is likely to be due to activities of other cytokines such as IL-17F (Fig. 4h, i). These data indicate that both T_{reg} and T_H17 cells contribute to preventing ILC3 activation: T_{reg} cells do so by decreasing IL-23 production from CCR2⁺ monocytes and monocyte-derived dendritic cells, whereas effector T cells regulate the bacterial burden. Both of these mechanisms prevent the activation of the IL-23–ILC3–IL-22–IEC circuit.

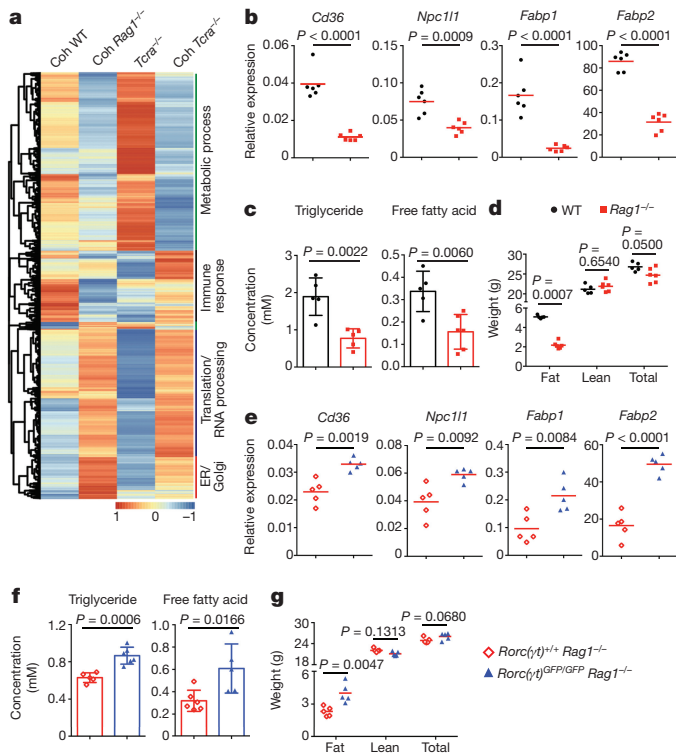


Figure 5 | Disrupted lipid metabolism in ILC3 and IEC-activated mice. **a**, RNA-seq analysis of ileal tissue from co-housed (Coh) wild-type, *Rag1*^{-/-} and *Tcra*^{-/-} mice and non-co-housed *Tcra*^{-/-} mice (*n* = 3). **b–g**, Expression of indicated genes (**b**, **e**), serum triglyceride and free fatty acid levels (**c**, **f**), and body composition (**d**, **g**) of wild-type (*n* = 5) or *Rag1*^{-/-} mice (*n* = 6) (**b–d**), and *Rorc*(γ)^{+/+}*Rag1*^{-/-} (*n* = 5) or *Rorc*(γ)^{GFP/GFP}*Rag1*^{-/-} mice (*n* = 5) (**e–g**). Results are representative of two independent experiments. Bars show mean (**b**, **d**, **e** and **g**) or mean \pm s.d. (**c** and **f**). Exact *P* values are given and calculated by two-tailed Student's *t*-test.

The evidence that ILC3s and adaptive lymphocytes operate sequentially and use markedly distinct effector mechanisms in their interactions with commensal bacteria raised the question of whether persistent ILC3 activity in the absence of adaptive immune control might have a negative effect on host homeostasis. To examine this issue, we performed whole-tissue RNA sequencing (RNA-seq) analysis of ilea from co-housed wild-type, *Rag1*^{-/-} and *Tcra*^{-/-} mice and separately housed *Tcra*^{-/-} mice. Genes that encode cytokines and anti-microbial peptides involved in microbial control were expressed at higher levels in pSTAT3⁺ *Rag1*^{-/-} and co-housed *Tcra*^{-/-} mice. By contrast, metabolic processing genes showed substantially lower expression in pSTAT3⁺ mice (Fig. 5a). Using quantitative real-time PCR (qPCR) analysis, we confirmed the reduction in mRNA coding for key lipid transporters, including *Cd36*, *Npc111*, *Fabp1* and *Fabp2*, in *Rag1*^{-/-} and co-housed *Tcra*^{-/-} mice (Fig. 5b and Extended Data Fig. 6a). This change was associated with significantly decreased serum levels of triglycerides and free fatty acids (Fig. 5c and Extended Data Fig. 6b). At the macroscopic level, *Rag1*^{-/-} mice exhibited less fat accumulation than wild-type mice that were fed a standard chow diet (Fig. 5d). Elimination of ILC3s in *Rorc*(γ)^{GFP/GFP}*Rag1*^{-/-} mice had the opposite effect, with higher levels of lipid transporters, serum triglycerides and free fatty acids, and higher fat storage than in *Rag1*^{-/-} mice with activated ILC3s (Fig. 5e–g). To investigate whether these lipid abnormalities were specifically associated with persistent IL-22 production, we administered adenoviruses expressing IL-22 or GFP to wild-type and non-co-housed *Tcra*^{-/-} mice. Injection of adenovirus expressing IL-22 induced notable STAT3 activation in IECs of wild-type mice, comparable to that seen in *Rag1*^{-/-} mice (Extended Data Fig. 7), and led to reduced expression of lipid transporters in the gut and lower

serum lipid concentration (Extended Data Fig. 6c–f). These findings suggest that, in the absence of adaptive lymphocytes, although ILCs are capable of constraining microbial communities their persistent activation results in abnormal lipid handling and tissue homeostasis. Previous studies suggested a role for IL-22 in lipid metabolism²⁶, with a recent report indicating that IL-22 promoted lipid transporter expression in IECs in the small intestine²⁷. It is likely that transient, low-level IL-22 production²⁷ has a notably different effect than the high-level, persistent exposure of IECs to this cytokine that we report here.

Previous studies of ILCs have focused on the roles of these cells in resistance to pathogens or in immunopathological conditions such as chronic inflammatory diseases⁶, with recent studies suggesting that they also have a role in neurobiological function^{28–30}. Here we demonstrate a clear role for these cells in the establishment of a compatible commensal state. Early in life, they temper the expansion of some bacterial species, especially those with inflammatory potential, protecting the epithelium of the gut. As the adaptive immune system matures, CD4⁺ T cells respond to the commensal population, and through mechanisms other than the IL-23-induced IL-22 pathway used by the ILC3s, establish a state of non-inflammatory commensalism in which the ILCs are largely quiescent. In the absence of a dominant adaptive immune response, the persistent activation of ILC3s results in impaired lipid metabolism. Our findings may have bearing on recent studies that show that a failure to develop a ‘mature’ gut microbiota is associated with severe nutritional abnormalities and other pathological states in humans as well as in germ-free animals colonized with microbial material from individuals with this condition^{31,32}. Taken together, our results increase understanding of how the innate and adaptive immune systems act sequentially on the developing gut microbiota to establish a balanced commensal state that supports normal tissue function.

Online Content Methods, along with any additional Extended Data display items and Source Data, are available in the online version of the paper; references unique to these sections appear only in the online paper.

Received 23 September 2016; accepted 6 December 2017.

Published online 22 January 2018.

- Caballero, S. & Pamer, E. G. Microbiota-mediated inflammation and antimicrobial defense in the intestine. *Annu. Rev. Immunol.* **33**, 227–256 (2015).
- Hooper, L. V., Littman, D. R. & Macpherson, A. J. Interactions between the microbiota and the immune system. *Science* **336**, 1268–1273 (2012).
- Belkaid, Y. & Hand, T. W. Role of the microbiota in immunity and inflammation. *Cell* **157**, 121–141 (2014).
- Renz, H., Brandtzaeg, P. & Hornef, M. The impact of perinatal immune development on mucosal homeostasis and chronic inflammation. *Nat. Rev. Immunol.* **12**, 9–23 (2011).
- Gensollen, T., Iyer, S. S., Kasper, D. L. & Blumberg, R. S. How colonization by microbiota in early life shapes the immune system. *Science* **352**, 539–544 (2016).
- Artis, D. & Spits, H. The biology of innate lymphoid cells. *Nature* **517**, 293–301 (2015).
- Bando, J. K. & Colonna, M. Innate lymphoid cell function in the context of adaptive immunity. *Nat. Immunol.* **17**, 783–789 (2016).
- Gerner, M. Y., Kastenmuller, W., Ifrim, I., Kabat, J. & Germain, R. N. Histocytometry: a method for highly multiplex quantitative tissue imaging analysis applied to dendritic cell subset microanatomy in lymph nodes. *Immunity* **37**, 364–376 (2012).
- Gerner, M. Y., Torabi-Parizi, P. & Germain, R. N. Strategically localized dendritic cells promote rapid T cell responses to lymph-borne particulate antigens. *Immunity* **42**, 172–185 (2015).
- Liu, Z. *et al.* Immune homeostasis enforced by co-localized effector and regulatory T cells. *Nature* **528**, 225–230 (2015).
- Nguyen, P. M., Putoczki, T. L. & Ernst, M. STAT3-activating cytokines: a therapeutic opportunity for inflammatory bowel disease? *J. Interferon Cytokine Res.* **35**, 340–350 (2015).
- Klose, C. S. *et al.* A T-bet gradient controls the fate and function of CCR6⁺ ROR- γ ⁺ innate lymphoid cells. *Nature* **494**, 261–265 (2013).
- Ivanov, I. I. *et al.* Induction of intestinal T_H17 cells by segmented filamentous bacteria. *Cell* **139**, 485–498 (2009).
- Sano, T. *et al.* An IL-23R/IL-22 circuit regulates epithelial serum amyloid A to promote local effector T_H17 responses. *Cell* **163**, 381–393 (2015).
- Guo, X. *et al.* Induction of innate lymphoid cell-derived interleukin-22 by the transcription factor STAT3 mediates protection against intestinal infection. *Immunity* **40**, 25–39 (2014).

16. Buonocore, S. *et al.* Innate lymphoid cells drive interleukin-23-dependent innate intestinal pathology. *Nature* **464**, 1371–1375 (2010).
17. Tamoutounour, S. *et al.* Origins and functional specialization of macrophages and of conventional and monocyte-derived dendritic cells in mouse skin. *Immunity* **39**, 925–938 (2013).
18. Jiang, H. Q., Bos, N. A. & Cebra, J. J. Timing, localization, and persistence of colonization by segmented filamentous bacteria in the neonatal mouse gut depend on immune status of mothers and pups. *Infect. Immun.* **69**, 3611–3617 (2001).
19. Goto, Y. *et al.* Segmented filamentous bacteria antigens presented by intestinal dendritic cells drive mucosal T_H17 cell differentiation. *Immunity* **40**, 594–607 (2014).
20. Yang, Y. *et al.* Focused specificity of intestinal T_H17 cells towards commensal bacterial antigens. *Nature* **510**, 152–156 (2014).
21. Eberl, G., Di Santo, J. P. & Vivier, E. The brave new world of innate lymphoid cells. *Nat. Immunol.* **16**, 1–5 (2015).
22. Fang, D. & Zhu, J. Dynamic balance between master transcription factors determines the fates and functions of CD4 T cell and innate lymphoid cell subsets. *J. Exp. Med.* **214**, 1861–1876 (2017).
23. Korn, L. L. *et al.* Conventional CD4⁺ T cells regulate IL-22-producing intestinal innate lymphoid cells. *Mucosal Immunol.* **7**, 1045–1057 (2014).
24. Littman, D. R. & Rudensky, A. Y. T_H17 and regulatory T cells in mediating and restraining inflammation. *Cell* **140**, 845–858 (2010).
25. Fontenot, J. D., Rasmussen, J. P., Gavin, M. A. & Rudensky, A. Y. A function for interleukin 2 in FOXP3-expressing regulatory T cells. *Nat. Immunol.* **6**, 1142–1151 (2005).
26. Wang, X. *et al.* Interleukin-22 alleviates metabolic disorders and restores mucosal immunity in diabetes. *Nature* **514**, 237–241 (2014). 10.1038/nature13564
27. Wang, Y. *et al.* The intestinal microbiota regulates body composition through NFIL3 and the circadian clock. *Science* **357**, 912–916 (2017).
28. Ibiza, S. *et al.* Glial-cell-derived neuroregulators control type 3 innate lymphoid cells and gut defence. *Nature* **535**, 440–443 (2016).
29. Cardoso, V. *et al.* Neuronal regulation of type 2 innate lymphoid cells via neuromedin U. *Nature* **549**, 277–281 (2017).
30. Klose, C. S. N. *et al.* The neuropeptide neuromedin U stimulates innate lymphoid cells and type 2 inflammation. *Nature* **549**, 282–286 (2017).
31. Blanton, L. V., Barratt, M. J., Charbonneau, M. R., Ahmed, T. & Gordon, J. I. Childhood undernutrition, the gut microbiota, and microbiota-directed therapeutics. *Science* **352**, 1533 (2016).
32. Subramanian, S. *et al.* Cultivating healthy growth and nutrition through the gut microbiota. *Cell* **161**, 36–48 (2015).

Supplementary Information is available in the online version of the paper.

Acknowledgements We thank Y. Choi and D.M. Kobuley for providing germ free *Rag1*^{-/-} mice and performing SFB mono-colonization; M. Oukka and S. K. Durum for providing mice; M. Mack, B. Gao and Y. Umesaki for providing anti-CCR2 antibody, IL-22 adenovirus and SFB faecal pellets; C. Eigsti, V. Nair and J. Davis for cell sorting, scanning electron microscopy and microbiota analysis; J. Zhu for discussions; and members of the Laboratory of Systems Biology for their comments during the course of these studies and input during preparation of this manuscript. Y.H. was supported by an NIAID K99 award (1K99AI123350-01A1). This research was supported by the Intramural Research Program of NIAID, NIH.

Author Contributions K.M. designed and conducted most of the experiments and data analysis and prepared the manuscript; A.P.B., S.T. and Y.H. helped with cell isolation and transfer; L.Z. measured mouse body composition; N.B. performed the analysis of microbiota translocation; A.J.M. performed the RNA-seq and data analysis; M.Y.G. provided helpful suggestions regarding imaging and histo-cytometry; Y.B. provided helpful suggestions, discussed data interpretation and contributed to the manuscript; and R.N.G. designed experiments, interpreted data and helped to write the manuscript.

Author Information Reprints and permissions information is available at www.nature.com/reprints. The authors declare no competing financial interests. Readers are welcome to comment on the online version of the paper. Publisher's note: Springer Nature remains neutral with regard to jurisdictional claims in published maps and institutional affiliations. Correspondence and requests for materials should be addressed to K.M. (kairui.mao@nih.gov) and R.N.G. (rgermain@nih.gov).

METHODS

Data reporting. Mice of similar ages were randomly allocated into different groups. For most experiments (co-housing, antibody treatment and cell transfer experiments), mice were ear-tagged with numbers and investigators did not know the identity of the specific samples until after data were analysed.

Mice. C57BL/6, *Rag1*^{-/-}, *Il23a*^{-/-}, *Foxp3*^{GFP}, *Tcrα*^{-/-}, *Ighm*^{-/-}, *B2m*^{-/-}, *H2-Ab1*^{-/-} and *H2-Ab1*^{-/-}*B2m*^{-/-} mice were obtained from Taconic Laboratories through a special NIAID contract. *Rorc*(γ)^{GFP/GFP}, *Il6*^{-/-} and 7B8-Tg mice were purchased from Jackson Laboratories. *Il22*-tdTomato mice were provided by S. K. Durum. *Il22*^{-/-} mice were provided by Genentech. Unless specified, mice used in the study were eight- to sixteen-week-old males. All mice were maintained in specific-pathogen-free conditions at an Association for Assessment and Accreditation of Laboratory Animal Care-accredited animal facility at the NIAID and were used under a study protocol approved by NIAID Animal Care and Use Committee (National Institutes of Health).

Germ-free *Rag1*^{-/-} mice were provided by the Penn Gnotobiotic Mouse Facility and experiments involving these mice were performed at the Penn Gnotobiotic Mouse Facility. Germ-free mice were maintained in sterile plastic isolator units and fed autoclaved LabDiet5021 mouse chow (LabDiet) and autoclaved water.

Immunofluorescence staining and confocal imaging. The ileal portion of the small intestine was excised and prepared using the Swiss roll technique, then incubated in a fixation and permeabilization solution (BD Bioscience, 554722) overnight followed by dehydration in 30% sucrose before embedding in OCT compound (Sakura Finetek). 18- μ m sections were cut on a CM3050S cryostat (Leica) and adhered to Superfrost Plus slides (VWR). Frozen sections were treated with methanol for 20 min at -20°C and then permeabilized and blocked in PBS containing 0.3% Triton X-100 (Sigma-Aldrich) and 10% normal mouse serum (Jackson Immunoresearch) followed by staining with antibodies diluted in blocking buffer. The following antibodies were used for staining: anti-CD3 (17A2; Biolegend), anti-EpCAM (G8.8, Biolegend), anti-ROR γ T (AFKJS-9, eBioscience), anti-CD90.2 (30-H12, Biolegend) and anti-pSTAT3 (D3A7, Cell Signaling Technology). After staining, slides were mounted with Fluormount G (Southern Biotech), and examined on a Leica TCS SP8 confocal microscope. Images were analysed with Imaris software (Bitplane).

Antibiotic treatment. Male six-week-old *Rag1*^{-/-} mice were provided with ampicillin (1 g/l), kanamycin (5 g/l), vancomycin (500 mg/l), neomycin trisulfate (1 g/l) and metronidazole (1 g/l) in drinking water for three weeks. All antibiotics were purchased from Sigma-Aldrich.

Histo-cytometry. Histo-cytometry analysis was performed as previously described⁸⁻¹⁰, with minor modifications. In brief, multi-parameter confocal images were corrected for fluorophore spillover using the Leica Channel Dye Separation module. For analysis of pSTAT3⁺ ILC3s, the ILC3 surface was constructed on the basis of the ROR γ T channel, and the object statistics were exported into FlowJo X (TreeStar) for analysis and graphing with Prism (GraphPad).

Co-housing and mono-colonization with SFB. Wild-type age-matched male mice were ear-tagged and housed in a cage with an equal number of the respective knockout mice for 4–8 weeks. For association of germ-free *Rag1*^{-/-} mice with SFB (a gift from Y. Umesaki), faecal pellets isolated from SFB mono-associated mice were reconstituted in sterile PBS and 200 μ l of this suspension was administered to each germ-free mouse by gavage in a sterile isolator. SFB reconstitution was confirmed by qPCR of faecal 16S ribosomal DNA relative to negative germ-free controls as previously described³³. Mono-associated mice were maintained for 3–4 weeks before analysis.

Lamina propria myeloid cell isolation. Small intestinal segments were treated with medium containing 5 mM EDTA and 0.145 mg/ml dithiothreitol for 30 min at 37°C with constant stirring. Tissue was further digested with 100 μ g/ml Liberase TL (Roche) and 500 μ g/ml DNase I (Sigma-Aldrich), with continuous stirring at 37°C for 30 min. Digested tissue was forced through a Collector tissue sieve (Bellco Glass) and passed through 70- and 40- μ m cell strainers. Cells were washed and incubated with a mixture of monoclonal antibodies containing anti-CD11c (N418, Biolegend), anti-MHC II (M5/114.15.2, eBioscience), anti-CD45(30-F11, BD Bioscience), anti-CD24 (M1/69, Biolegend), anti-CD64 (X54-5/7.1, Biolegend), anti-CCR2 (#475301, R&D Systems), anti-CD11b (M1/70, eBioscience), anti-Ly-6C (HK1.4, Biolegend) and anti-CD103 (2E7, eBioscience), as well as monoclonal antibodies against the non-dendritic-cell components: anti-Ly-6G (1A8, BD Biosciences), anti-NK1.1 (PK136, BD Biosciences), anti-TCR β (H57-597, BD Biosciences), anti-TCR $\gamma\delta$ (GL3, BD Biosciences), anti-Siglec F (E50-2440, BD Biosciences) and anti-B220 (RA3-6B2, BD Biosciences). Different myeloid-cell populations were sorted by flow cytometry on a FACSAria. Purity was verified by flow cytometry on a FACSAria. The purity of all populations was > 99%.

Adoptive transfer and antibody treatment. CD4⁺ T cells were isolated from lymph nodes and spleens from wild-type or *Foxp3*^{GFP} mice using the CD4⁺

T Cell Isolation Kit (Miltenyi, 130-104-454). T_{reg} cells were sorted according to GFP expression, and 1 \times 10⁷ total CD4⁺ T cells or 1 \times 10⁶ T_{reg} cells were transferred into *Rag1*^{-/-} mice intravenously. Naive T cells from 7B8-Tg mice or from CBir1-Tg mice were isolated using the naive CD4⁺ T cell Kit (Miltenyi, 130-104-453) and transferred into *Rag1*^{-/-} mice intravenously (1 \times 10⁶ cells per mouse) for 6–8 weeks.

IL-2-IL-2-antibody complexes were made by mixing 1 μ g recombinant mouse IL-2 (Biolegend) with 5 μ g anti-IL-2 monoclonal antibody (clone JES6-1, BioXcell) followed by incubation at 37°C for 30 min. Mice were injected intraperitoneally with IL-2-IL-2-antibody complexes, 150 μ g anti-IL-17A (Clone 17F3, BioXcell) or isotype control IgG twice a week after T-cell transfer. For monocyte depletion, *Rag1*^{-/-} mice were injected intraperitoneally with 20 μ g anti-CCR2 (clone MC-21, a gift from M. Mack), 200 μ g anti-Gr1 (clone RB6-8C5, BioXcell) or isotype control IgG on days 0, 1, 2, 3, 5, 7, 9, 11 and 13. Mice were euthanized 24 h after the last injection.

Quantitative real-time PCR. RNA from the terminal ileum was isolated with Trizol reagent (Thermo Fisher Scientific). cDNA was synthesized using the iScript cDNA Synthesis kit (Bio-Rad) according to the manufacturer's instructions. qPCR was performed using SsoFast EvaGreen Supermixes (Bio-Rad) or LightCycler 480 Probes Master (Roche). Reactions were run with the CFX Connect Real-Time PCR Detection System (Bio-Rad). The primer and probe set for *mIl23p19* (Mm00518984) was purchased from Thermo Fisher Scientific. See Extended Data Table 1 for a list of primers and probes used in this study.

Analysis of microbiota in the small intestine. The contents of the small intestine were collected from different mice, and bacterial DNA was extracted with the QIAamp DNA Stool Kit (QIAGEN) according to the manufacturer's instructions. Different species of bacteria were quantified by qPCR with primers specific for 16S rRNA genes using SsoFast EvaGreen Supermixes (Bio-Rad). See Extended Data Table 1 for a list of primers.

Scanning electron microscopy. Mouse terminal ilea (immediately proximal to the ileal-caecal junction) were collected, slit and fixed overnight in fresh fixative. All subsequent processing was carried out in a Pelco Biowave microwave (TedPella) at 250 W under 15-inch Hg vacuum. The tissue pieces were washed in 0.1 M sodium cacodylate buffer and post-fixed in 1% osmium tetroxide reduced with 0.8% potassium ferrocyanide in 0.1 M sodium cacodylate buffer. After three washes with buffer, the tissue pieces were dehydrated in a graded ethanol series and dried using a Bal-Tec 030 critical point dryer. The tissue pieces were subsequently coated with 70 Å iridium using ion-beam sputtering (South Bay Technology) and imaged using a SU-8000 scanning electron microscope (Hitachi).

RNA-seq analysis. Total RNA was extracted from distal small intestine using TRIzol (Thermo Fisher Scientific). RNA-seq libraries were prepared using the Illumina TruSeq Stranded LT mRNA library preparation kit (Illumina), and libraries were sequenced on an Illumina NextSeq 500 to a read depth of 25–35 million reads per sample. Sequencing quality control was assessed using FastQC version 0.11.3 (<http://www.bioinformatics.babraham.ac.uk/projects/fastqc/>). Reads were mapped to the UCSC mm9 *Mus musculus* genome using Tophat2³⁴ with the following flags: -library-type fr-firststrand -r 25. The tool featureCounts from the subread³⁵ Python package was used to count reads mapping to gene features, and the R package DEseq2_ENREF_38³⁶ was used to test for differential expression and to generate regularized log-transformed (rlog) count tables. The R package pheatmap was used to generate the heatmap of the RNA-seq results, and ggplot2 was used to generate scatterplots of the rlog counts.

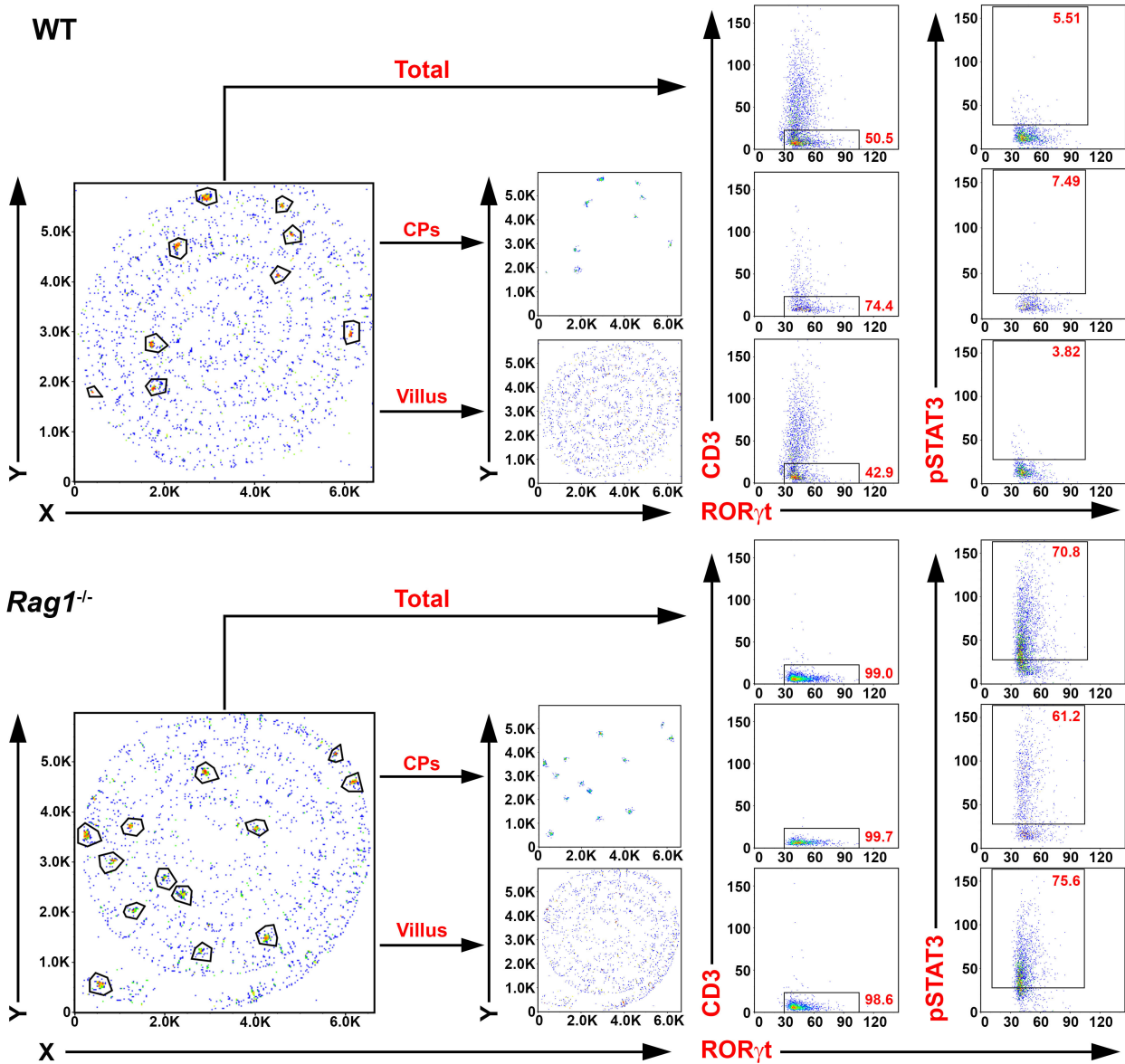
Serum triglycerides, free fatty acids and body composition measurement. Serum triglycerides and free fatty acids were measured using a Triglyceride Reagent Set (Pointe Scientific, Inc.) and Free Fatty Acid Quantitation Kit (Sigma-Aldrich) according to the manufacturer's instructions. Mouse body composition, including fat and lean masses, was measured with EchoMRI at four months of age.

Administration of mice with IL-22 adenovirus. Adenoviruses expressing IL-22 and GFP were provided by B. Gao. IL-22 adenovirus was made by cloning mouse IL-22 cDNA (544 bp) into the pENTR/D-TOPO system (Invitrogen), followed by using the Gateway system (Invitrogen) to perform an LR reaction with pAd/CMV/V5-DEST to make the expression vector pAd/CMV/mIL-22. Mice were injected intravenously with 2 \times 10⁸ pfu IL-22 adenovirus or GFP adenovirus.

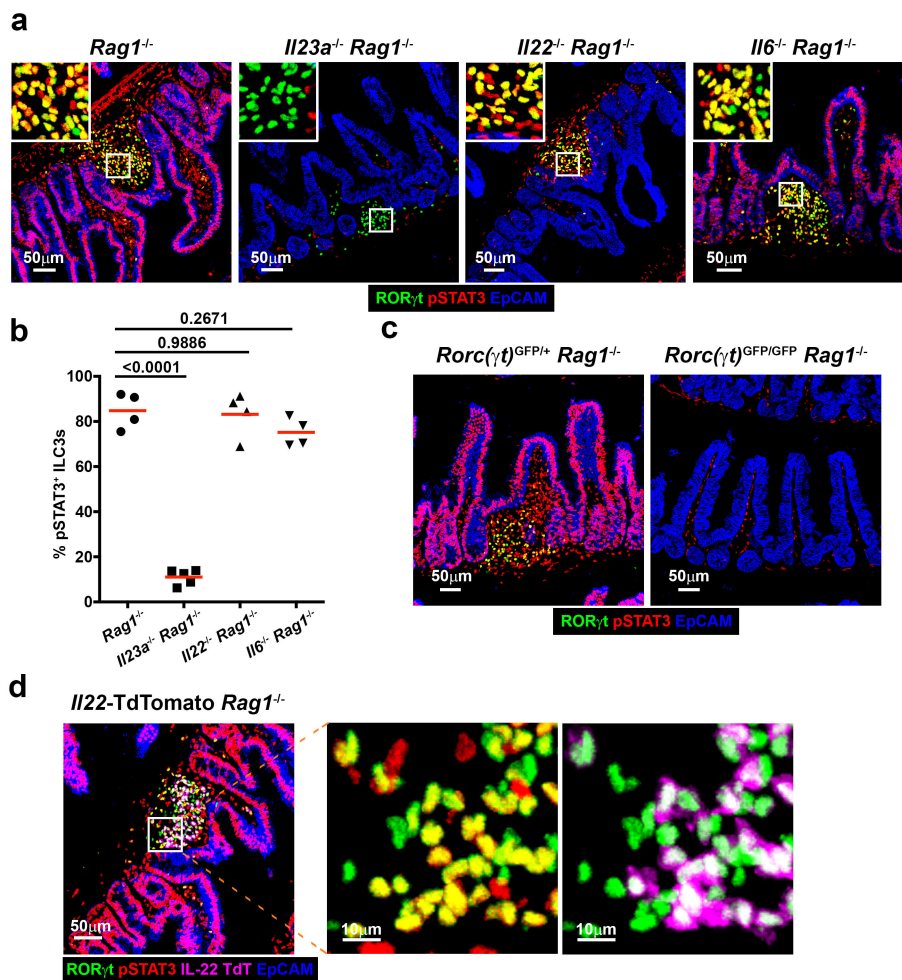
Statistical analysis. No statistical methods were used to predetermine sample size. Prism software (GraphPad) was used for all statistical analysis. Student's *t*-test (two-tailed), or one-way or two-way ANOVA were used for the statistical analysis of differences between two groups; *****P* < 0.0001, and exact *P* values are shown in figures.

Data availability. RNA-seq data that support the findings of this study have been deposited in the Gene Expression Omnibus database with the accession number GSE86780. Figure 5a shows RNA-seq-related data. The data that support the findings of this study are available from the corresponding author upon reasonable request.

33. Qiu, J. *et al.* Group 3 innate lymphoid cells inhibit T-cell-mediated intestinal inflammation through aryl hydrocarbon receptor signaling and regulation of microflora. *Immunity* **39**, 386–399 (2013).
34. Kim, D. *et al.* TopHat2: accurate alignment of transcriptomes in the presence of insertions, deletions and gene fusions. *Genome Biol.* **14**, R36 (2013).
35. Liao, Y., Smyth, G. K. & Shi, W. featureCounts: an efficient general purpose program for assigning sequence reads to genomic features. *Bioinformatics* **30**, 923–930 (2014).
36. Love, M. I., Huber, W. & Anders, S. Moderated estimation of fold change and dispersion for RNA-seq data with DESeq2. *Genome Biol.* **15**, 550 (2014).

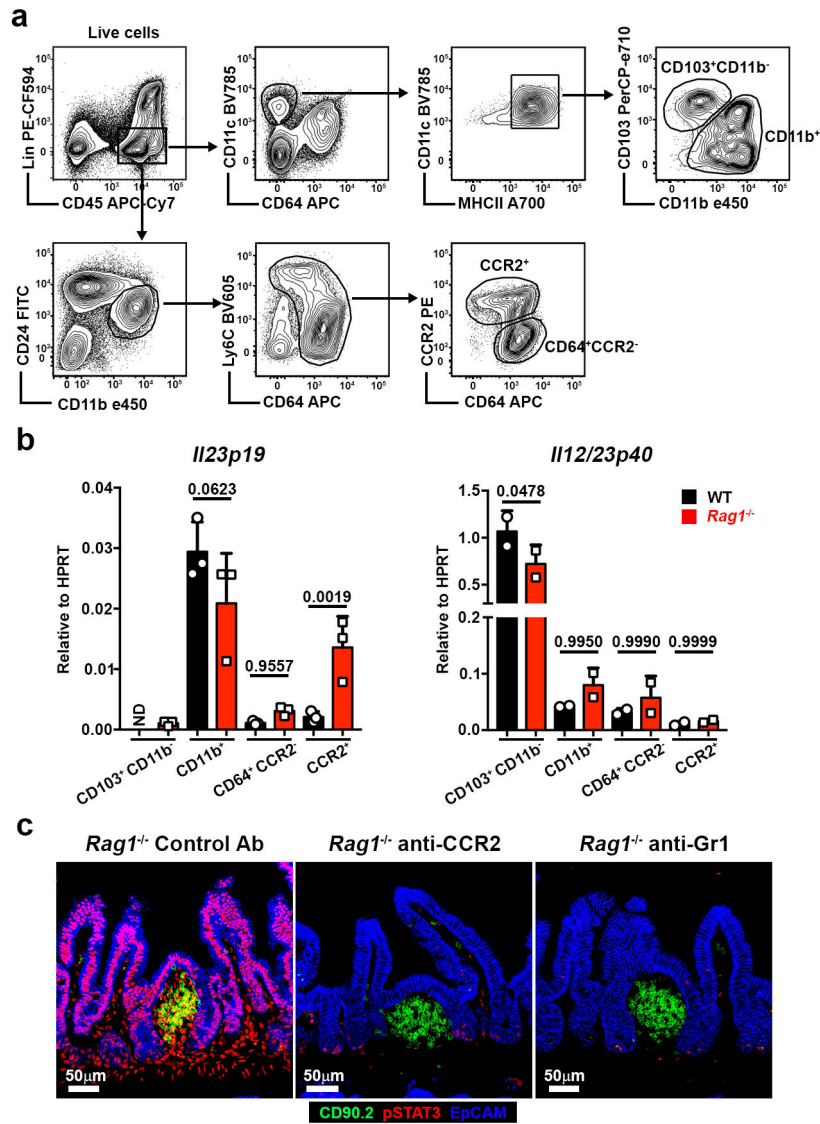


Extended Data Figure 1 | Quantification of pSTAT3⁺ ILC3s by histo-cytometry. Gating strategy for analysis of pSTAT3⁺ ILC3s from small intestine of wild-type or Rag1^{-/-} mice.



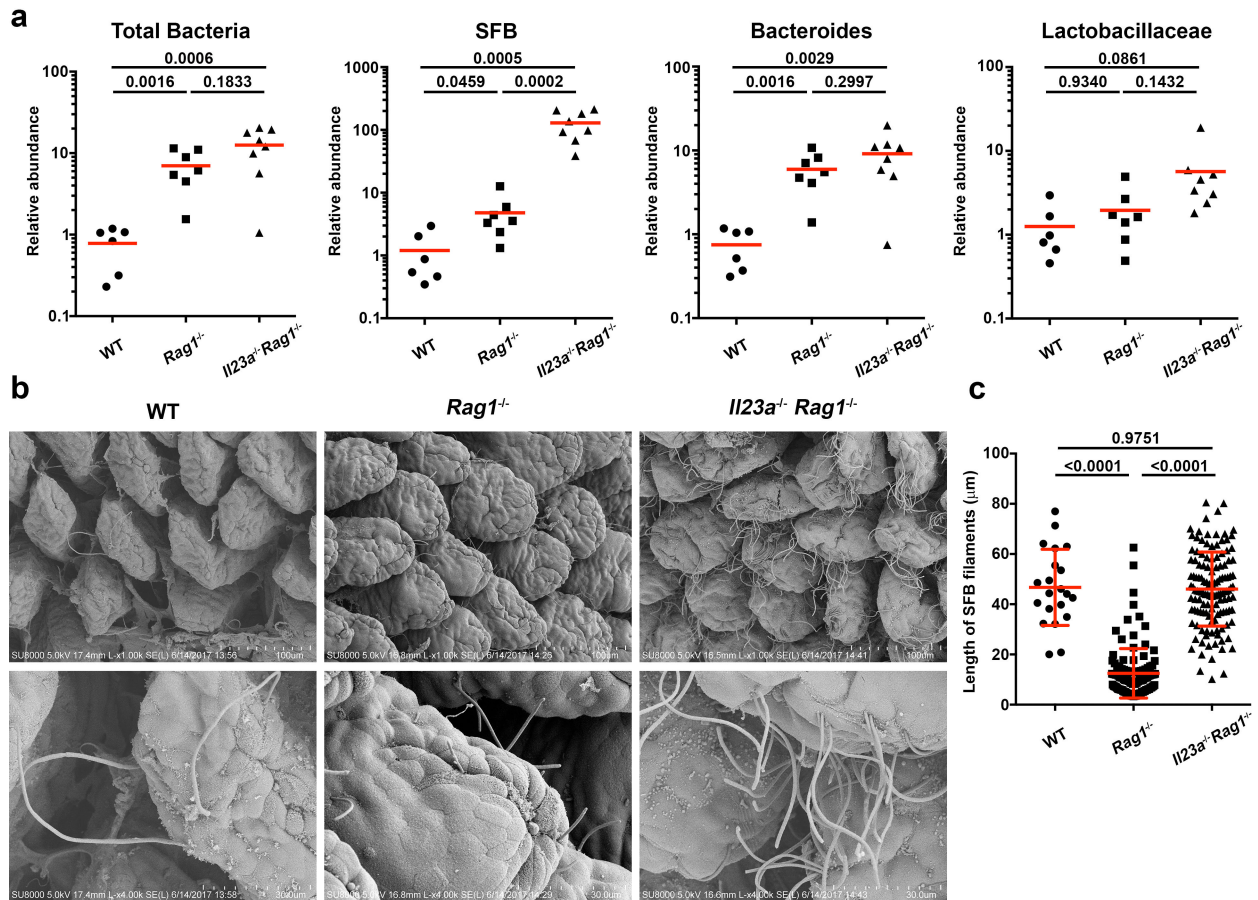
Extended Data Figure 2 | Cellular and molecular mechanism of STAT3 activation in *Rag1^{-/-}* small intestine. **a**, Immunofluorescence staining of ileum from *Rag1^{-/-}* ($n = 4$), *Il23a^{-/-}Rag1^{-/-}* ($n = 5$), *Il22^{-/-}Rag1^{-/-}* ($n = 4$) and *Il6^{-/-}Rag1^{-/-}* mice ($n = 4$). **b**, Percentage of pSTAT3⁺ ILC3s in **a**. **c–d**, Immunofluorescence staining of ileum from

Rorc(γt)^{GFP/+}Rag1^{-/-} and *Rorc(γt)^{GFP/GFP}Rag1^{-/-}* mice ($n = 4$; **c**) and *Il22-tdTomato Rag1^{-/-}* mice ($n = 3$; **d**). Results are representative of three independent experiments. Bars show mean; exact P values are given and calculated by one-way ANOVA.



Extended Data Figure 3 | Mononuclear phagocyte subpopulation responsible for IL-23 production and pSTAT3 activation. **a**, Flow cytometry of total live cells from the small intestine lamina propria, showing the gating strategy for sorting different myeloid-cell subsets: CD103⁺CD11b⁻ and CD11b⁺ conventional dendritic cells, CD64⁺CCR2⁻ macrophages and CCR2⁺ monocytes and monocyte-derived dendritic cells.

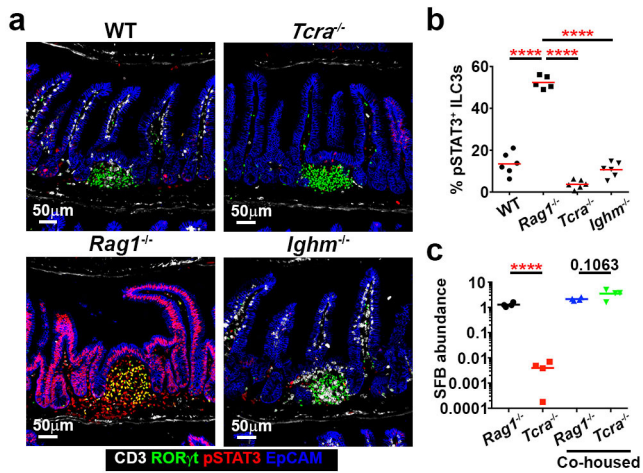
b, Expression of *Il23a* ($n = 3$) and *Il12b* (which encodes the p40 subunit of IL-12) in different cell populations sorted as in **a** ($n = 2$). **c**, Immunofluorescence staining of ileum from *Rag1*^{-/-} mice and *Rag1*^{-/-} mice treated with anti-CCR2 or anti-Gr1 antibody for two weeks ($n = 4$). Results are representative of three independent experiments. Mean \pm s.d.; exact P values are given and calculated by two-way ANOVA.



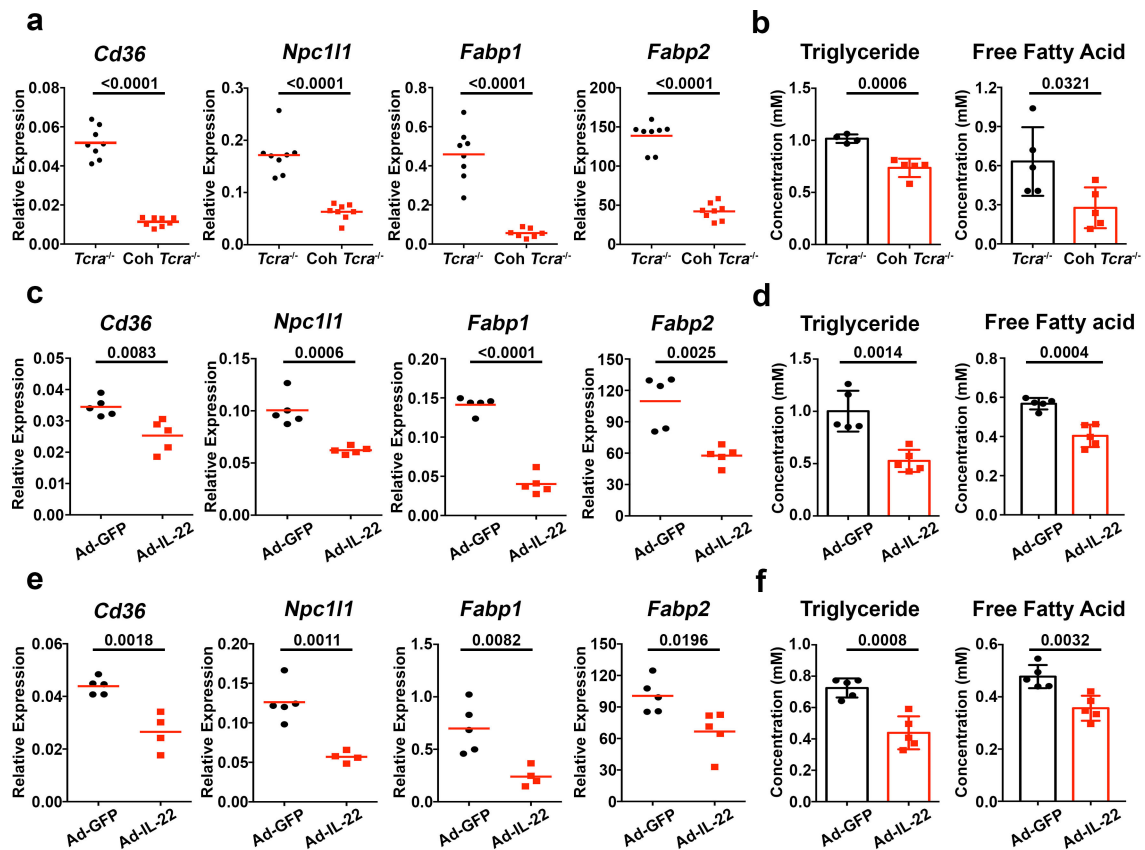
Extended Data Figure 4 | Microorganisms in the small intestine of co-housed wild-type, *Rag1*^{-/-} and *Il23a*^{-/-} *Rag1*^{-/-} mice.

a, Quantification of indicated bacteria species in the ileum of co-housed wild-type ($n = 6$), *Rag1*^{-/-} ($n = 7$) and *Il23a*^{-/-} *Rag1*^{-/-} ($n = 8$) mice by real-time PCR with primers specific to 16S rRNA genes. Results are pooled

from two independent experiments. **b**, Scanning electron microscopy of terminal ileum of co-housed mice as in **a** ($n = 3$). **c**, Quantification of the length of SFB filaments in **b**. Results are representative of two independent experiments. Bars show mean (**a**) and mean \pm s.d. (**c**); exact P values are given and calculated by one-way ANOVA.

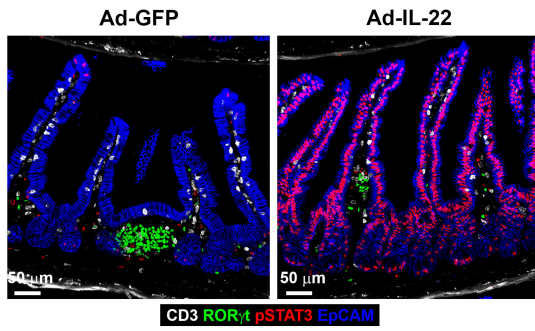


Extended Data Figure 5 | Lack of ILC3 activation in SFB negative *Tcra*^{-/-} mice. **a**, Immunofluorescence staining of ileum from wild-type ($n = 6$), *Rag1*^{-/-} ($n = 5$), *Tcra*^{-/-} ($n = 5$) and *Ighm*^{-/-} mice ($n = 6$). **b**, Percentage of pSTAT3⁺ ILC3s in **a**. **c**, Quantification of SFB in distal small intestine of non-co-housed *Rag1*^{-/-} and *Tcra*^{-/-} or co-housed *Rag1*^{-/-} and *Tcra*^{-/-} mice ($n = 4$). Results are representative of three (**a**, **b**) or two (**c**) independent experiments. Bars show mean; **** $P < 0.0001$; otherwise exact P values are shown and calculated by one-way ANOVA.



Extended Data Figure 6 | Dysregulation of lipid metabolism by IL-22.
a, Expression of indicated genes in the ileum from age-matched male $Tcra^{-/-}$ mice and $Tcra^{-/-}$ mice co-housed with $Rag1^{-/-}$ mice ($n = 8$). Results are pooled from two independent experiments. **b**, Serum triglyceride and free fatty acid levels from $Tcra^{-/-}$ mice and $Tcra^{-/-}$ mice co-housed with $Rag1^{-/-}$ mice ($n = 5$). **c–f**, Expression of indicated genes in

the ileum (**c, e**) and serum triglyceride and free fatty acid levels (**d, f**) from wild-type (**c, d**) or $Tcra^{-/-}$ mice (**e, f**) injected with adenovirus expressing IL-22 ($n = 5$) or GFP ($n = 5$). Results are representative of two independent experiments. Bars show mean (**a, c, e**) and mean \pm s.d. (**b, d, f**); exact P values are given and calculated by two-tailed Student's t -test.



Extended Data Figure 7 | STAT3 activation in IECs by IL-22 adenovirus. Immunofluorescence staining of ileum from C57BL/6 mice injected with adenoviruses expressing either IL-22 or GFP for two weeks. Images are representative of three sections from three mice of each group and results are representative of two independent experiments.

Extended Data Table 1 | Primers and probes for quantitative PCR

| | |
|-----------------------|-----------------------------|
| <i>Hprt</i> FW | TGAAGAGCTACTGTAATGATCAGTCA |
| <i>Hprt</i> RV | AGCAAGCTTGCAACCTTAACCA |
| <i>Il22</i> FW | CATGCAGGAGGTGGTACCTT |
| <i>Il22</i> RV | CAGACGCAAGCATTCTCAG |
| <i>Reg3b</i> FW | ATGGCTCCTACTGCTATGCC |
| <i>Reg3b</i> RV | GTGTCCTCCAGGCCTCTT |
| <i>Reg3g</i> FW | CAAGGTGAAGTTGCCAAGAA |
| <i>Reg3g</i> RV | CCTCTGTTGGGTTTCATAGCC |
| <i>SAA1/2</i> FW | CTGCCTGCCAATACTGAGAGTC |
| <i>SAA1/2</i> RV | CCACTTCCAAGTTCCTGTTTATTAC |
| <i>Eubacteria</i> FW | ACTCCTACGGGAGGCAGCAGT |
| <i>Eubacteria</i> RV | ATTACCGCGGCTGCTGGC |
| <i>SFB</i> FW | GACGCTGAGGCATGAGAGCAT |
| <i>SFB</i> RV | GACGGCACGGATTGTTATTCA |
| <i>Bacteroides</i> FW | GGTTCGAGAGGAGGTCCC |
| <i>Bacteroides</i> RV | GCTGCCTCCCGTAGGAGT |
| <i>Hprt</i> FW | TGGATATGCCCTTGACTATAATGAG |
| <i>Hprt</i> RV | TGGCAACATCAACAGGACTC |
| <i>Hprt</i> Probe | TCAACTTGCCTCATCTTAGGCTTTGTA |
| <i>Cd36</i> FW | GCGACATGATTAATGGCACAG |
| <i>CD36</i> RV | GATCCGAACACAGCGTAGATAG |
| <i>CD36</i> Probe | CAACAAAAGGTGGAAAGGAGGCTGC |
| <i>Npc1l1</i> FW | CGGAACTCACAGGACTTTACAG |
| <i>Npc1l1</i> RV | TGCTGGTAGAACACATTGGAG |
| <i>Npc1l1</i> Probe | AGCTGAACTACGGAAGGTGCCTG |
| <i>Fabp1</i> FW | TCTCCGGCAAGTACCAATTG |
| <i>Fabp1</i> RV | TTGATGTCCTTCCCTTTCTGG |
| <i>Fabp1</i> Probe | TGAATGGCTCAAAGTTCTCCTGGCT |
| <i>Fabp2</i> FW | AGCTCGGTGTAACCTTTCCC |
| <i>Fabp2</i> RV | TTCATTACCAGAACTCTCGG |
| <i>Fabp2</i> Probe | TTATTTCCCTCAATGGTCCAGGCC |
| <i>Il12p40</i> FW | GGCTGGTGCAAGAAACATGGACT |
| <i>Il12p40</i> RV | AGAGACGCCATTCCACATGTCACT |
| <i>Il12p40</i> Probe | TCAACATCAAGAGCAGTAGCAGTTCCC |

Life Sciences Reporting Summary

Nature Research wishes to improve the reproducibility of the work that we publish. This form is intended for publication with all accepted life science papers and provides structure for consistency and transparency in reporting. Every life science submission will use this form; some list items might not apply to an individual manuscript, but all fields must be completed for clarity.

For further information on the points included in this form, see [Reporting Life Sciences Research](#). For further information on Nature Research policies, including our [data availability policy](#), see [Authors & Referees](#) and the [Editorial Policy Checklist](#).

► Experimental design

1. Sample size

Describe how sample size was determined.

No statistical methods were used to predetermine sample size.

2. Data exclusions

Describe any data exclusions.

No samples were excluded from analysis.

3. Replication

Describe whether the experimental findings were reliably reproduced.

Experiments were repeated and our data are based on at least two to three independent experiments with similar results. The precise number of repeats are given in the figure legend.

4. Randomization

Describe how samples/organisms/participants were allocated into experimental groups.

Mice of similar ages were randomly allocated into different groups.

5. Blinding

Describe whether the investigators were blinded to group allocation during data collection and/or analysis.

For most experiments, mice were ear-tagged with simple numbers. The person who performed the experiments did not know the identity of the specific samples until after data were analyzed.

Note: all studies involving animals and/or human research participants must disclose whether blinding and randomization were used.

6. Statistical parameters

For all figures and tables that use statistical methods, confirm that the following items are present in relevant figure legends (or in the Methods section if additional space is needed).

n/a Confirmed

- The exact sample size (n) for each experimental group/condition, given as a discrete number and unit of measurement (animals, litters, cultures, etc.)
- A description of how samples were collected, noting whether measurements were taken from distinct samples or whether the same sample was measured repeatedly
- A statement indicating how many times each experiment was replicated
- The statistical test(s) used and whether they are one- or two-sided (note: only common tests should be described solely by name; more complex techniques should be described in the Methods section)
- A description of any assumptions or corrections, such as an adjustment for multiple comparisons
- The test results (e.g. P values) given as exact values whenever possible and with confidence intervals noted
- A clear description of statistics including central tendency (e.g. median, mean) and variation (e.g. standard deviation, interquartile range)
- Clearly defined error bars

See the web collection on [statistics for biologists](#) for further resources and guidance.

► Software

Policy information about [availability of computer code](#)

7. Software

Describe the software used to analyze the data in this study.

Imaris x64 7.7 and 8.1 for image analysis; GraphPad Prism 6 and 7 for statistics; Flowjo 10.1 for histo-cytometry analysis; FastQC, Tophat2, FeatureCounts, R package DEseq2, pheatmap and ggplot2 for RNAseq analysis.

For manuscripts utilizing custom algorithms or software that are central to the paper but not yet described in the published literature, software must be made available to editors and reviewers upon request. We strongly encourage code deposition in a community repository (e.g. GitHub). *Nature Methods* [guidance for providing algorithms and software for publication](#) provides further information on this topic.

► Materials and reagents

Policy information about [availability of materials](#)

8. Materials availability

Indicate whether there are restrictions on availability of unique materials or if these materials are only available for distribution by a for-profit company.

IL-22 deficient mice are available upon reasonable request from Genentech. SFB fecal pellets are available upon reasonable request from Yakult Central Institute. The adenovirus are available upon reasonable request from Dr. Bin Gao. Anti-CCR2 antibody is available upon reasonable request from Dr. Matthias Mack. All other materials are commercially available.

9. Antibodies

Describe the antibodies used and how they were validated for use in the system under study (i.e. assay and species).

Following antibodies were used in this study: anti-CD3 (17A2, BV-421,100228; Alexa-647, 100209), anti-EpCAM (G8.8, Alexa-488, 118210; Alexa594, 118222; Alexa-647, 118212), anti-CD90.2 (30-H12, Alexa488, 105315), anti-CD24 (M1/69, FITC, 101806), anti-CD11c (N418, BV785,117336), anti-CD64 (X54-5/7.1, APC, 139306) and anti-Ly6C (HK1.4, BV605, 128036) were purchased from BioLegend. Anti-RORgt (AFKJS-9, 14-6988-82), anti-CD11b (M1/70, eFlour450, 48-0112-82), anti-CD103 (2E7, PerCP-eFlour710, 46-1031-82) and anti-MHCII (M5/114.15.2, Alexa700, 56-5321-82) were purchased from eBiosciences. Anti-CD45 (30-F11, APC-Cy7, 557659), anti-TCRb (H57-597, PE-CF594, 562841), anti-B220 (RA3-6B2, PE-CF594, 562290), anti-TCRgd (GL3, PE-CF594, 563532), anti-NK1.1 (PK136, PE-CF594, 562864) and anti-Siglec-F (E50-2440, PE-CF594, 562757) were purchased from BD Biosciences. Anti-CCR2 (#475301, PE, FAB5538P-100) was purchased from R&D System. Anti-Phospho-Stat3 (D3A7, 9145L) was purchased from Cell Signaling Technology. Anti-GFP (Alexa488, A21311), Goat anti-Rat IgG (Alexa488, A11006; Alexa647, A21247) and Goat anti-Rabbit IgG (Alexa 568, A11011) were purchased from Thermo Fisher Scientific. Anti-IL-2 (JES6-1A12, BE0043), anti-IL-17A (17F3, BE0173), anti-Gr-1 (RB6-8C5, BE0075) and isotype control antibody (LTF-2, BE0090) were purchased from BioXcell. All the reagents were optimized and validated by the companies.

10. Eukaryotic cell lines

a. State the source of each eukaryotic cell line used.

No eukaryotic cell lines were used.

b. Describe the method of cell line authentication used.

No eukaryotic cell lines were used.

c. Report whether the cell lines were tested for mycoplasma contamination.

No eukaryotic cell lines were used.

d. If any of the cell lines used are listed in the database of commonly misidentified cell lines maintained by [ICLAC](#), provide a scientific rationale for their use.

No eukaryotic cell lines were used.

► Animals and human research participants

Policy information about [studies involving animals](#); when reporting animal research, follow the [ARRIVE guidelines](#)

11. Description of research animals

Provide details on animals and/or animal-derived materials used in the study.

C57BL/6, Rag1^{-/-}, Il23a^{-/-}, Foxp3-GFP, Tcra^{-/-}, Ighm^{-/-}, B2m^{-/-}, H2-Ab1^{-/-} and H2-Ab1^{-/-} B2m^{-/-} mice were obtained from Taconic Laboratories through a special NIAID contract. Rorc(gt)GFP/GFP, Il6^{-/-} and 7B8 TCR Tg mice were purchased from Jackson Laboratories. Il22-tdTomato mice were kindly provided by Dr. Scott K. Durum (National Cancer Institute, National Institutes of Health). Il22^{-/-} mice were kindly provided by Genentech. Germ-free animals were provided by the Penn Gnotobiotic Mouse Facility. All mice used were on a C57BL/6 genetic background and were 8-16 weeks-old male mice, unless specified.

Policy information about [studies involving human research participants](#)

12. Description of human research participants

Describe the covariate-relevant population characteristics of the human research participants.

This study did not involve human research participants.

Flow Cytometry Reporting Summary

Form fields will expand as needed. Please do not leave fields blank.

► Data presentation

For all flow cytometry data, confirm that:

- 1. The axis labels state the marker and fluorochrome used (e.g. CD4-FITC).
- 2. The axis scales are clearly visible. Include numbers along axes only for bottom left plot of group (a 'group' is an analysis of identical markers).
- 3. All plots are contour plots with outliers or pseudocolor plots.
- 4. A numerical value for number of cells or percentage (with statistics) is provided.

► Methodological details

- 5. Describe the sample preparation.
- 6. Identify the instrument used for data collection.
- 7. Describe the software used to collect and analyze the flow cytometry data.
- 8. Describe the abundance of the relevant cell populations within post-sort fractions.
- 9. Describe the gating strategy used.

Tick this box to confirm that a figure exemplifying the gating strategy is provided in the Supplementary Information.